UNIVERSITEIT•STELLENBOSCH•UNIVERSITY
jou kennisvennoot • your knowledge partner

A Multiplexed Impedance Analyser for Biosensing Applications

Karl Voigt
24867209

Report submitted in partial fulfilment of the requirements of the module Project (E) 448 for the degree Baccalaureus in Engineering in the Department of Electrical and Electronic Engineering at Stellenbosch University.

Supervisor: Dr T. Ebrahim

October 2025

Acknowledgements

I would like to thank my dog, Muffin. I also would like to thank the inventor of the incubator; without him/her, I would not be here. Finally, I would like to thank Dr Herman Kamper for this amazing report template.

UNIVERSITEIT•STELLENBOSCH•UNIVERSITY
jou kennisvennoot • your knowledge partner

Plagiaatverklaring / *Plagiarism Declaration*

1. Plagiaat is die oorneem en gebruik van die idees, materiaal en ander intellektuele eiendom van ander persone asof dit jou eie werk is.
   Plagiarism is the use of ideas, material and other intellectual property of another's work and to present is as my own.

2. Ek erken dat die pleeg van plagiaat 'n strafbare oortreding is aangesien dit 'n vorm van diefstal is.
   I agree that plagiarism is a punishable offence because it constitutes theft.

3. Ek verstaan ook dat direkte vertalings plagiaat is.
   I also understand that direct translations are plagiarism.

4. Dienooreenkomstig is alle aanhalings en bydraes vanuit enige bron (ingesluit die internet) volledig verwys (erken). Ek erken dat die woordelikse aanhaal van teks sonder aanhalingstekens (selfs al word die bron volledig erken) plagiaat is.
   Accordingly all quotations and contributions from any source whatsoever (including the internet) have been cited fully. I understand that the reproduction of text without quotation marks (even when the source is cited) is plagiarism

5. Ek verklaar dat die werk in hierdie skryfstuk vervat, behalwe waar anders aangedui, my eie oorspronklike werk is en dat ek dit nie vantevore in die geheel of gedeeltelik ingehandig het vir bepunting in hierdie module/werkstuk of 'n ander module/werkstuk nie.
   I declare that the work contained in this assignment, except where otherwise stated, is my original work and that I have not previously (in its entirety or in part) submitted it for grading in this module/assignment or another module/assignment.

Studentenommer / *Student number*	Handtekening / *Signature*
Voorletters en van / *Initials and surname*	Datum / *Date*

Abstract

English

The English abstract.

Afrikaans

Die Afrikaanse uittreksel.

Contents

List of Figures

List of Tables

Nomenclature

Variables and functions

$p(x)$	Probability density function with respect to variable x.
$P(A)$	Probability of event A occurring.
ε	The Bayes error.
ε_u	The Bhattacharyya bound.
B	The Bhattacharyya distance.
s	An HMM state. A subscript is used to refer to a particular state, e.g. s_i refers to the i^{th} state of an HMM.
$\mathbf{S}$	A set of HMM states.
$\mathbf{F}$	A set of frames.
$\mathbf{o}_f$	Observation (feature) vector associated with frame f.
$\gamma_s(\mathbf{o}_f)$	A posteriori probability of the observation vector $\mathbf{o}_f$ being generated by HMM state s.
μ	Statistical mean vector.
Σ	Statistical covariance matrix.
$L(\mathbf{S})$	Log likelihood of the set of HMM states $\mathbf{S}$ generating the training set observation vectors assigned to the states in that set.
$\mathcal{N}(\mathbf{x}\|\mu, \Sigma)$	Multivariate Gaussian PDF with mean μ and covariance matrix Σ.
a_{ij}	The probability of a transition from HMM state s_i to state s_j.
N	Total number of frames or number of tokens, depending on the context.
D	Number of deletion errors.
I	Number of insertion errors.
S	Number of substitution errors.

Acronyms and abbreviations

ADC analogue-to-digital converter

CPE constant phase element

DAC digital-to-analogue converter

DUT device-under-test

EIS electrochemical impedance spectroscopy

EMI electromagnetic interference

GBW gain-bandwidth product

LPF low-pass filter

MCU microcontroller unit

MUX multiplexer

PGA programmable gain amplifier

POC point-of-care

TIA transimpedance amplifier

Chapter 1

Introduction

1.1. Background

Biosensors are defined as devices that measures biological and chemical reactions through the use of a physical transducer mechanism which in turn generates signals porportional to the concentration of an analyte in a sample. [4] This allows for the detection of various biological elements such as biomarkers which can be used to monitor health conditions or diagnose diseases.

Designing a low-cost easy to use device to take readings from biosensors, would thus provide a valuable tool for the early screening of diseases such as cancer. Changing wording and goals to be focused on point of care screening rather than analysis/detection

This would decrease the need for expensive labratory testing and allow for lower cost and more regular testing of patients using a point-of-care device. Having a multiplexed device, able to take readings from multiple biosensors, would allow a single blood sample to be taken and multiple tests to be run on it with minimum involvement from a healthcare professional.

1.2. Project Objectives

This is a multifaceted project that aims to develop a low-cost, easy-to-use device for reading biosensors. The system design objectives for the device include:

- Developing a circuit that allows a microcontroller to read a biosensor through the use of Electrochemical Impedance Spectroscopy (EIS). This entails conditioning the sinusoidal signal generated by a DAC and measuring the current response from the biosensor through an ADC.
- This measurement circuitry needs to be multiplexed to allow for multiple biosensors to be read in turn without the need for human intervention.
- The microcontroller should be able to filter and process the biosensor data to determine the concentration of the analyte in the sample.

- The device needs to be able to communicate these results in a clear and user-friendly manner. This will be done through the use of a LCD screen on the device as well as a web interface that can be accessed through a smartphone or computer.
- The device should be battery powered, low-cost and easy to use, thus allowing for widespread adoption and use in various environments.

1.3. Project Scope

NOT THE DESIGN OF Biosensors NOT TESTING WITH REAL BLOOD (We arent qualified for that)

1.4. Chapter Overview

Chapter 1: Introduction

Provides an overview of the motivation, background, objectives, scope, and structure of the report.

Chapter 2: Literature Review

Reviews relevant research and technologies in speech recognition and neural networks.

Chapter 3: Methodology

Describes the methods and approaches used in the project, including data collection and model development.

Chapter 4: Experiments and Results

Presents experimental setup, results, and analysis.

Chapter 5: Discussion

Discusses findings, limitations, and implications of the results.

Chapter 6: Conclusion and Future Work

Summarizes the work and suggests directions for future research.

Chapter 2

Literature Review

2.1. Biosensors

Biosensors are employed in applications such as disease monitoring, drug discovery, and detection of pollutants, disease-causing micro-organisms and markers that are indicators of a disease in bodily fluids (blood, urine, saliva, sweat). [4]

2.1.1. Background on Biomarkers

A biomarker is an objective measure that that gives an indication of the biological processes happening inside the body at a given moment. [5] They are physical substances found in the body that can be measured. The concentration of biomarkers differs between healthy individuals and individuals with diseases, thereby aiding in diagnosis and monitoring of diseases. [6] Some biomarkers are easy to measure (such as blood pressure, body weight, etc.) while others require tests of blood, urine or tissue samples. [5]

This project will focus on the detection of biomarkers found in blood samples such as the CA-19 biomarker used for pancreatic cancer detection. Note: Verduidelik bietjie oor CA-19. The concentration of these biomarkers in blood can give an indication of the presence and progression of a variety of diseases, including many types of cancer. [7]

2.1.2. Types of Biosensors

A biosensor consists of an analyte, a bioreceptor and a transducer mechanism combined with the electronics needed to process the signal. [4] The analyte is the substance of interest (such as biomarkers) that needs detection. Bioreceptors are molecules such as enzymes, cells, DNA or antibodies that specifically recognise the analyte. These bioreceptors produce a signal (in the form of light, heat, pH, charge or mass change, etc.) when they interact with the analyte. [4] Antibody based biosensors are the type of biosensor that will be used to detect biomarkers in this project.

Antibodies are produced by vertebrates as part of their immune response to foreign organisms or substances (called antigens). They are the most common biorecognition element used in biosensors. [8] Antibodies are Y-shaped cells that can be divided into two

distinct regions. The top of the Y is variable and binds to a specific antigen depending on the amino acids present in this region. The amino acids present in the constant region (the bottom of the Y) is similar between different classes of antibodies (within the same species of animal). [8] This constant region binds to the substrate of the biosensor during immobilization, leaving the variable region free to bind with antigens. [9]

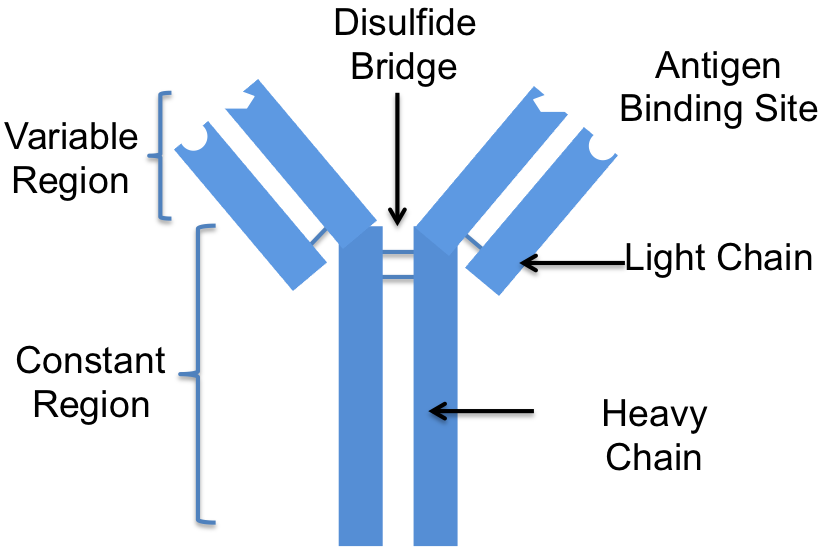

Figure 2.1: Antibody with basic structural features labeled [10]

Many biosensors require that a ”label” is attached to the biomolecule of interest and then the concentration of this label is detected and extrapolated to the concentration of the biomolecule [11]. Label-free biosensors, on the other hand, directly detect the target biomolecule by measuring the changes in electrical properties of the surface of the biosensor when binding occurs. Since labeling can dramatically alter the binding properties of biomolecules and adds complexity and cost to the assay process, label-free detection is highly desirable [11], especially in point-of-care environments.

2.2. Transducer Mechanisms

The number of biological binding events indicates the concentration of the analyte in the sample. In order to convert the bio-recognition event into a measurable signal, a transducer mechanism is needed [4]. There are various types of transducer mechanisms that can be used in biosensors, including optical, piezoelectric and electrochemical transducers. This project will focus on biosensors where binding events change the electrical properties of the biosensor, specifically the complex impedance. Thus, electrochemical transducers are of interest.

Electrochemical transducers can use various analysis techniques. In potentiometric analysis, the potential of an electrode is measured against a reference electrode at zero-current [12]. Coulometry applies a constant potential (with regards to a reference electrode)

onto an electrode surface to carry out exhaustive electrolysis of an analyte [12]. Voltammetry involves subjecting the sample to a varying potential at the electrode's surface and measuring the resulting Faradaic current [12]. Finally there is electrochemical impedance spectroscopy (EIS), which measures the complex impedance of an electrochemical system as a function of frequency [12]. EIS is particularly suitable for biosensor applications where biological binding events alter the electrical properties of the electrode-electrolyte interface [11].

2.2.1. Electrochemical Impedance Spectroscopy (EIS)

EIS involves applying a small sinusoidal perturbation to the device-under-test (DUT) and measuring the response. This can be either a voltage or current signal, while the other is measured. By varying the frequency of the excitation signal, different electrochemical processes that occur at distinct time constants can be characterised.

EIS relies on the system acting as a linear time-invariant system, but most real-world electrochemical systems are inherently nonlinear [13]. To approximate linear behaviour and ensure valid results, EIS uses a small AC excitation signal, typically between 1–10 mVpp [14] [13]. At higher amplitudes, the response deviates from ideal sinusoidal form, causing harmonic distortion and invalid measurements. However, making the excitation too small reduces signal-to-noise ratio, so 10 mVpp is commonly used to balance linearity and measurement quality. A key advantage of EIS is the ability to simulate the electrochemical system using equivalent circuit models. These models represent the various resistive, capacitive, and diffusive elements that represent the behaviour of the system [13]. This is due to the frequency domain nature of EIS, in comparison with other techniques such as voltammetry that works in the time-domain, thus allowing the behaviour of distinct processes that dominate at certain frequencies to be characterised [13]. By fitting experimental impedance data to these models, parameters such as charge transfer resistance and double-layer capacitance can be extracted, which correlate with biomolecular interactions occurring on the electrode surface [11]. This capability makes EIS a powerful tool for label-free biosensing applications.

2.2.2. Faradaic vs Non-Faradaic EIS Sensors

EIS biosensors can be categorized into two main types based on their transduction mechanism: faradaic and non-faradaic sensors.

In faradaic measurements, charge transfers occur at the electrode-solution interface and redox reactions occur on the electrode surface [15]. The equivalent circuit model for faradaic sensors is the Randles circuit (Figure 2.2a), consisting of solution resistance (R_s) in series with the parallel combination of charge transfer resistance (R_{CT}) and double-layer capacitance (C_{dl}), plus Warburg impedance (Z_w) representing diffusion processes [15].

Non-faradaic measurements operate without charge-transfer reactions, functioning as capacitive sensors that detect changes in the electrical double layer capacitance. Due to the lack of charge-transfer, R_{CT} becomes infinitely large, thus creating an open circuit [15]. On solid electrodes, the observed impedance response of C_{DL} differs from an ideal capacitor, thus a constant phase element (CPE) is used instead of C_{DL} in the Randles non-fardaic equivalent circuit (Figure 2.2b).

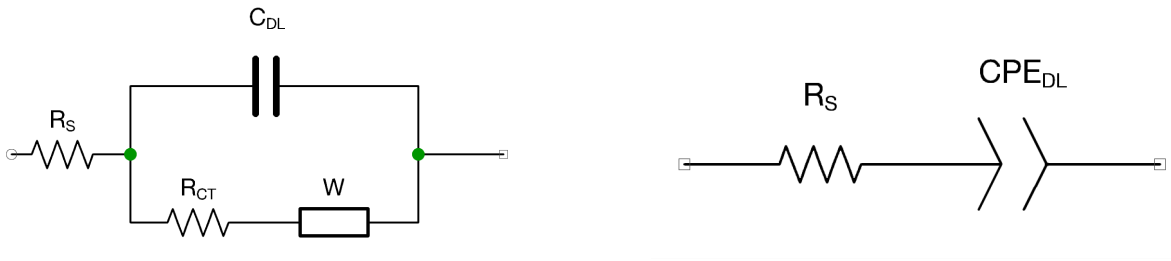

(a) Faradaic Randles Circuit **(b)** Non-Faradaic Randles Circuit

Figure 2.2: Equivalent Circuits for Faradaic and Non-Faradaic EIS Biosensors

2.3. Complex Impedance

Electrochemical impedance spectroscopy (EIS) produces complex impedance data consisting of both magnitude and phase information across a range of frequencies. The complex impedance is calculated as:

$$Z(\omega) = \frac{V(\omega)}{I(\omega)} = Z'(\omega) + jZ''(\omega) \tag{2.1}$$

where $Z'(\omega)$ is the real component representing resistive behaviour and $Z''(\omega)$ is the imaginary component representing capacitive or inductive behaviour (with $V(\omega)$ and $I(\omega)$ representing the phasor voltage and current respectively) [13].

Two major ways of visualizing this complex impedance are the Nyquist and Bode representations, each highlighting different aspects of the electrochemical response.

2.3.1. Nyquist Plot

A Nyquist plot displays the negative imaginary part of impedance($Z''(\omega)$) versus the real part ($Z'(\omega)$) [16]. Each point on the plot corresponds to a particular frequency, though the frequency is not explicitly shown along the axes. For biosensing, high-frequency data points are located near the origin (low impedance), while low-frequency points are farther along the curve (high impedance). The Nyquist plot has the distinct advantage that some circuit parameters can be read directly form the plot [16].

A purely resistive impedance is represented as a point on the x-axis, as it has no imaginary component and is not frequency dependent. A purely capacitive impedance on the other hand is represented as a straight vertical line on the y-axis, as it has no real component and its imaginary component varies inversely with frequency [16]. The series combination of resistive and capacitive elements, thus result in a vertical line offset from the y-axis. The parallel combination of resistive and capacitive elements, however result in a semicircular arc, as current flows though the path of least resistance [16]. At low frequencies, the capacitor acts as an open circuit resulting in the x-axis intercept (or diameter of the semi-circle) representing the magnitude of the resistive elements in the circuit.

For simple electrochemical systems such as a Randles cell, the Nyquist plot appears as a semicircle (frequencies where charge transfer phenomena dominate) ending in a straight line tail (frequencies where mass transfer phenomena dominate) (Figure 2.3) [13]. The series resistance (R_s) can be read directly from the x-axis intercept at high frequencies (closer to the origin), while the charge transfer resistance (R_{CT}) is given by the diameter of the semicircle in middle frequencies. At low frequencies, the Warburg impedance (Z_w) manifests as a 45-degree line due to diffusion-limited processes [13], explaining the observed tail.

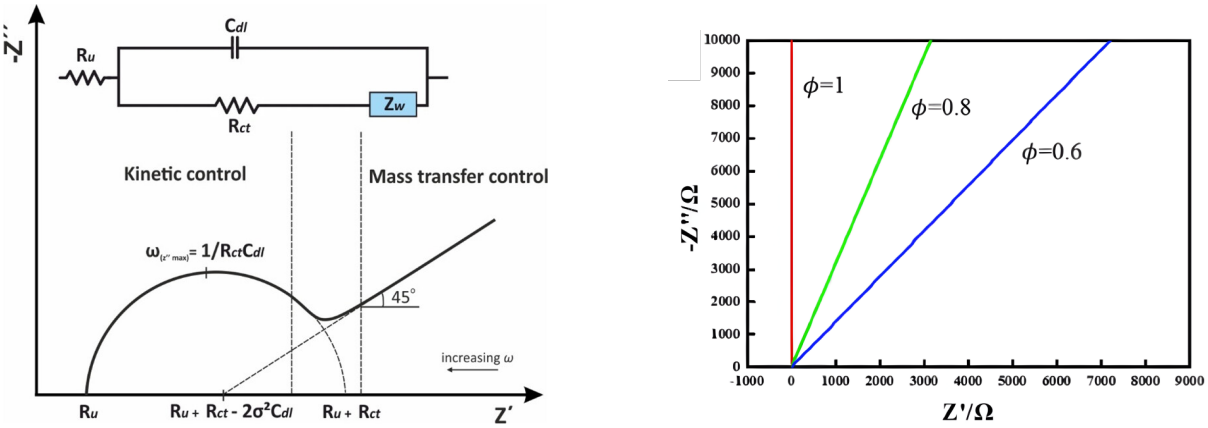

(a) Faradaic Randles Circuit [13] **(b)** Non-Faradaic Randles Circuit [15]

Figure 2.3: Nyquist Plots of Faradaic and Non-Faradaic Randles Circuits

The non-faradaic Randles equivalent, however does not exhibit a semi-circle, due to the exclusion of the charge transfer resistance (R_{CT}) and Warburg impedance (Z_w). Instead, the Nyquist plot appears as a straight line with an x-axis intercept representing R_S. For solid electrodes, however the line is not vertical as would be expected from the series combination of a resistive and purely capacitive element [15] (Figure 2.3b). The C_{DL} is thus replaced with a CPE in the circuit model to account for this non-ideal capacitive behaviour. The impedance of the CPE is given by equation 2.2, with ω representing the angular frequency, T being a constant related to capacitance, and α being an exponent between 0 and 1 that characterizes the deviation from ideal capacitive behaviour [15]. α

corresponds to the angle of the line in the Nyquist plot. When $\alpha = 1$, the CPE behaves as an ideal capacitor, while values less than 1 indicate increasing non-ideality due to factors such as surface roughness or inhomogeneities [15].

$$Z_{CPE} = \frac{1}{T(j\omega)^{\alpha}} \tag{2.2}$$

2.3.2. Bode Plots

A Bode plot presents the magnitude, $|Z|$, and phase, ϕ, of the impedance as functions of frequency on a logarithmic scale. The Bode magnitude plot reveals how impedance changes with frequency, while the phase plot shows the transition between resistive ($\phi = 0°$) and capacitive ($\phi = -90°$) behaviour. While Nyquist plots offer direct visualization of resistive and capacitive interactions, Bode plots highlight the frequency dependence and allow clearer distinction of time constants [16]. In EIS analysis, both representations are complementary: Nyquist plots assist model-based fitting, whereas Bode plots verify consistency and highlight transition frequencies.

2.4. Impedance Analysers

Impedance analysers are instruments that integrate signal generation, voltage and current measurement, and data processing to determine the complex impedance of a DUT. In the context of biosensing, these devices are used to perform EIS by applying a known AC excitation signal to the biosensor and measuring the resulting current and voltage responses over a range of frequencies. The ratio of these phasor quantities provides the frequency-dependent impedance, which is used to infer biochemical interactions at the electrode–electrolyte interface.

There are numerous commercial EIS solutions available, such as the PalmSens4, Gamry Reference 600+, and Metrohm Autolab PGSTAT. These instruments are designed for research and industrial applications where extremely high accuracy, broad frequency ranges, and advanced analytic capabilities are essential.

For instance, the PalmSens4 can measure impedances over frequencies from 10 Hz to 1 MHz, with 18-bit resolution, integrated equivalent circuit fitting, and software for parameter extraction. However, such instruments are prohibitively expensive—often exceeding, (≈€4200). These devices also require significant technical expertise to interpret Nyquist and Bode plots or analyse equivalent circuit models, making them unsuitable for low-resource POC settings where portability, cost, and ease of use are crucial.

For these reasons, miniaturised, low-cost impedance analysers are being actively developed for POC applications such as [17], [18] and [19]. Such designs prioritise simplicity,

automation, and affordability, while maintaining sufficient frequency range and measurement accuracy to detect biological binding events.

2.4.1. Signal Generation

EIS requires the generation of a small AC excitation signal, either voltage or current, to probe the DUT. Generating or measuring voltage is simple as most modern electronics are voltage mode rather than current mode. On the other hand, generating a small current signal is difficult to do accurately and requires circuits such as the improved Howlard current pump [20]. While measuring a current signal also has some complexity, it is significantly easier than generation and thus the method commonly used in EIS systems.

Voltage based signal generation can be done using dedicated impedance analyser chips such as the AD5933 or custom solutions using microcontroller-based digital-to-analogue converters (DACs). The AD5933 offers integrated frequency sweeps and impedance measurement. However, it has some clear drawbacks, such as a DC offset, lack of direct voltage measurement and minimum impedance of $1k\Omega$.

Direct measurement of the true voltage across the device under test ensures all sources of non-ideal behaviour (parasitic resistances, stray capacitance, drift, and environmental changes) are accounted for, providing accurate data for impedance calculation. Accurate voltage monitoring is vital because small changes can significantly affect calculated impedance, particularly in low-voltage biosensing circuits. In contrast, a DAC and ADC solution implemented on a microcontroller allows for precise control of excitation signals, flexible signal processing, and easier integration with multiplexing and user interface subsystems

2.4.2. Voltage Measurement

2.4.3. Current Measurement

2.5. Related Works

Chapter 3

Design

3.1. Design Philosophy

The aim of this project is to design a impedance spectroscopy system that can be used in a point-of-care setting. Tim Brown's design thinking principles [21] are thus well suited and were used as the bases for the design process. Brown's approach is characterised by five stages: empathising with the end user, defining a clear problem statement, ideating a wide range of creative ideas, building a quick prototype, and finally testing. These phases are cyclical and allow rapid iteration and learning. This project represents the culmination of this design process, although further iterations of the design process could allow further refinement of the end product.

3.1.1. Understanding the end user

Point-of-care (POC) diagnostic devices are essential for decentralized healthcare, particularly in resource-limited settings such as rural clinics and community health facilities. While EIS has proven to be a powerful technique for biosensing applications, existing solutions present significant barriers to widespread adoption in POC environments.

Commercial impedance analysers such as the PalmSens4 offer exceptional technical capabilities, including frequency ranges from 10 µHz to 1 MHz, high resolution (18-bit), and data analysis features such as circuit modelling [22]. However, these instruments have two critical limitations for POC applications. Firstly, they require substantial technical expertise to interpret EIS data, as users must understand the underlying electrochemical principles to extract meaningful diagnostic information. Secondly, commercial systems like the PalmSens4 are prohibitively expensive, with prices €15,000, making them impractical for widespread deployment in clinics, rural health centres, or low-resource settings.

Previous academic projects have successfully demonstrated low cost impedance spectroscopy devices [23] [18] [17], but similarly require users to manually analyse impedance spectra and possess an understanding of EIS principles to interpret the results. This technical barrier prevents POC personnel from using these devices effectively.

POC healthcare providers require a device that performs impedance-based biosensing but abstracts the complexity away from the user, presenting results in an intuitive way.

Quantitative results, rather than qualitative results are sufficient to indicate the need for referral to a specialist and further testing.

3.1.2. Problem Statement

How can we design a low-cost, easy-to-use impedance analyzer for biosensing applications that eliminates the need for specialized knowledge, enabling point-of-care personnel to test for multiple biomarkers?
This problem statement encapsulates three critical design requirements :

1. Accessibility: The device must process raw impedance measurements and convert them to meaningful outputs, removing the need for users to understand Nyquist plots, equivalent circuit models, or phase angle analysis. Running from a battery and being able to operate without a computer are also necessities in rural settings.

2. Affordability: The total system cost must remain under R4,500 (approximately €220), making it orders of magnitude more affordable than commercial alternatives like the PalmSens4 at €15,000, thereby enabling widespread deployment in resource-limited settings.

3. Multiplexing capability: In resource constrained POC environments, healthcare professionals often face high patient loads. Due to this, multiplexed POC testing is of increasing importance for clinical screening [24]. This allows the screening of multiple analytes with minimal involvement from healthcare professionals.

3.2. Functional Design Overview

The system can be broken up into multiple subsystems, each fulfilling a specific function in order to create a complete device that meets the requirements. On the most basic level the device consists of the DUTs, an impedance analyser and a user interface. The DUT is the biosensor that interacts with the analyte and whose impedance characteristics change based on the analyte concentration. A multiplexer is used to interface between multiple DUT's and the impedance analyser. The impedance analyser can be further broken down into the power electronics, excitation stage, voltage and current measurement stages and finally the processing that uses an STM32. The user interface is based on an ESP32 and communicates with the impedance analyser through UART.

Breek impedance analyser op in further subsystems Discuss wat ons wil bereik en hoe ons dit gan opbreek. Beskryf hoe die circuit die beginsels van biosensors en EIS in ag moet neem, basies wat dit moet doen, hoekom multiplexing en ja dan hoe daai overall doel in gedeeltes opgebreek word.

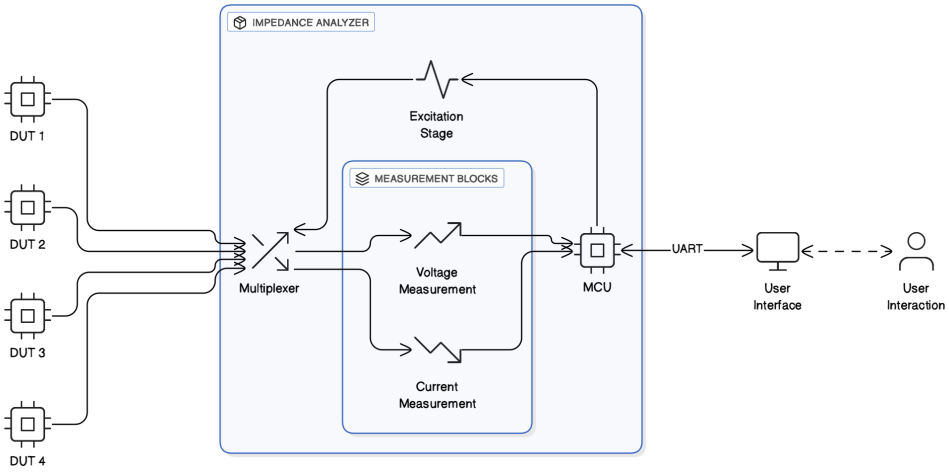

Figure 3.1: System Overview

3.3. Subsystem Design

3.3.1. Excitation

The easiest way of producing a controlled voltage signal is using a DAC. Both dedicated DACs and DACs built into microcontroller units (MCUs) were possible options.

Biosensing requires a bipolar signal with no DC component to avoid charge accumulation at the electrode–electrolyte interface, which leads to polarization. Over time, this would establish a net electrochemical bias, which drives redox reactions and changes the interfacial chemistry of the biosensor. These parasitic reactions alter the impedance characteristics of the electrode, obscuring the true dielectric and charge transfer properties that the EIS measurement aims to quantify. This can be solved by shifting our generated excitation to be biased around ground using a level shifting op-amp circuit. However, this also requires providing all analogue circuitry with a negative supply rail. Rather, this project makes use of a buffered virtual ground reference at 1.65V (3.3V/2) and uses this as the midpoint for all the analogue circuitry. This approach ensures that no DC bias is applied to the DUT while negating the need for negative supply rails.

When generating a sinusoidal signal using a DAC, the output is not a smooth analogue waveform, but rather a series of discrete voltage steps. These steps introduce high-frequency components and harmonics that are not present in the original signal. If these unwanted frequencies are not removed, they can interfere with downstream analogue circuitry or be misinterpreted during subsequent analog-to-digital conversion, a phenomenon known as aliasing. To prevent this, an anti-aliasing filter (AA filter), typically a low-pass filter (LPF), is placed after the DAC output to remove high-frequency content and smooth out the signal.

Dynamic range determines the smallest signal the DAC can produce above its noise floor.

The theoretical dynamic range (in dB) of a DAC is given by the following formula [25]:

$$\text{Dynamic Range} = 6.02n + 1.76 \tag{3.1}$$

with n being the number of bits of resolution. For the 12-bit DAC found in the STM32F303K8, this results in a dynamic range of 74dB. When designing the AA filter, the dynamic range determines the required level of attenuation at the Nyquist frequency ($f_s/2$). To prevent high-frequency components—introduced by the DAC's discrete step output—from being aliased back into the signal band, the AA filter must attenuate these frequencies sufficiently so that any aliased content falls below the DAC's noise floor, as set by its dynamic range. At the same time, the filter's passband must remain flat at the desired signal bandwidth to avoid distorting the amplitude or phase of the intended output.

If we want to have more calculations insert, the calcs of how to calculate the cutoff of an 8th order raised cosine to have -74dB at fs/2 but it's going to be at least 1/2 page

Due to these requirements, a fixed frequency AA filter is unsuitable when generating a wide range of frequencies from 1Hz-100kHz. Many variable AA filter ICs exist, however many require changing a resistor value to set the cutoff frequency. This would be impractical when many frequencies are needed. Ultimately the LTC1069 proved to be the only viable option, providing an 8th order lowpass filter that approximates a raised cosine response (with $\alpha = 1$). Importantly it has a cutoff frequency of up to 120kHz (200kHz when using $\pm 5V$ supply rails) set by an external clock and a linear phase response [26]. The clock-tunable nature of the LTC1069 is ideal for this project, allowing easy adjustments through the use of a timer on the STM.

To maximise the voltage resolution and minimise noise, the full linear range of the DAC is utilised when generating the signal. This requires that our DAC output signal is attenuated from 3Vpp to the desired 10mVpp using an inverting op-amp. From equation 3.2 $R_f = 1k\Omega$ and $R_{in} = 300k\Omega$ can be calculated as suitable values.

$$A_v = \frac{V_{out}}{V_{in}} = -\frac{R_f}{R_{in}} \tag{3.2}$$

Insert diagrams of stair stepping and frequency components. Dalk sommer van LT Spice

3.3.2. Voltage Measurement

Some impedance analyser designs attempt to infer voltage across the sample by using the known attenuation an applied signal [17]. However, direct measurement of the true voltage across the device under test ensures all sources of non-ideal behaviour (parasitic resistances, stray capacitance, drift, and environmental changes) are accounted for, providing accurate

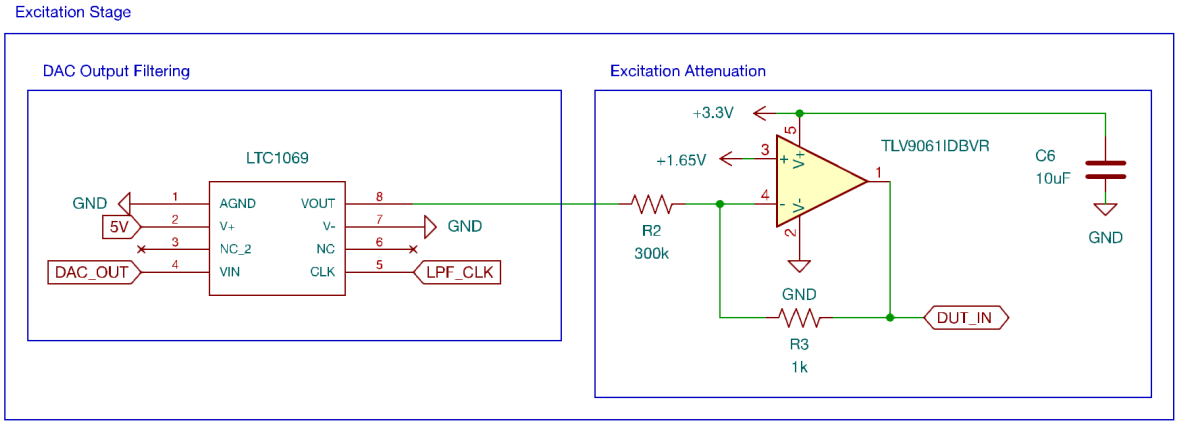

Figure 3.2: Complete Excitation Stage Circuit

data for impedance calculation. Accurate voltage monitoring is vital because small changes can significantly affect calculated impedance, particularly in low-voltage biosensing circuits.

It is essential to measure the voltage directly across the biosensor, rather than measuring the applied signal only in reference to the virtual ground. This ensures that variations that occur due to the dynamic and non-ideal behaviours at the sensor–electrolyte interface are included, leading to more reliable results.

Two common circuits are used to achieve this: differential op-amps and instrumentation amplifiers. Differential op-amps are simple and cost-effective for basic differential measurements, but they are susceptible to common-mode noise and offset errors [27]. Differential op-amps also have low input impedance, which loads the signal source and can affect test results [27]. Instrumentation amplifiers, on the other hand, are specifically designed for high-precision differential measurement and provide superior common-mode rejection, high input impedance and excellent accuracy even when the input signals are small or operating in a noisy environment [28]. This makes instrumentation amplifiers particularly suitable for biosensing applications where the signals to be measured can be very small, and minimizing interference is critical.

Additionally, it is important to amplify the measured voltage to fully utilise the linear range of the analogue-to-digital converter (ADC), which enhances both sensitivity and resolution. By maximizing the voltage swing within the ADC's input range, the system can discriminate smaller changes in sensor response, thus allowing for better detection of low-concentration analytes.

Gain-bandwidth product (GBW) represents the -3dB bandwidth of an op-amp at unity gain. The -3dB bandwidth of the op-amp can then be calculated for a specific gain using equation 3.3 where A_{noise} represents the noise gain calculated in equation 3.4. The use of noise gain accounts for the non-ideal feedback effects and circuit imperfections [29].

$$f_c = \frac{GBW}{A_{noise}} \tag{3.3}$$

$$A_{noise} = 1 + \frac{R_f}{R_{in}} \tag{3.4}$$

The gain and phase shift at any frequency can then be calculated based on the cutoff frequency using equations 3.5 and 3.6 respectively [30]. With $\omega = 2\pi f$ and $\omega_0 = 2\pi f_c$.

$$|H(j\omega)|_{dB} = 20 \log \frac{1}{\sqrt{1 + \frac{\omega^2}{w_0^2}}} \tag{3.5}$$

$$\varphi(\omega) = -\tan^{-1}(\frac{\omega}{\omega_0}) \tag{3.6}$$

Using a single stage of amplification to amplify the signal from 10mVpp back to 3Vpp would introduce significant phase shifts and gain reductions at higher test frequencies. This is alleviated by using a two stage amplification design. The INA331 instrumentation amplifier was selected for the first stage of voltage measurement due to its combination of low offset voltage, high common-mode rejection and low input bias current. The INA331 features a typical offset voltage of 250 µV, which represents the inherent DC error between the input terminals when no differential signal is applied. It directly adds to the measured voltage, creating a systematic DC error that must be considered in calibration. The low input bias current of 0.5pA avoids loading the DUT and influencing our current measurements. The device provides an internal gain of 5 V/V, configurable to higher gains through external resistors according to the relationship $G = 5 + 5 \times \frac{R_2}{R_1}$. Choosing $R_1 = 1k\Omega$ and $R_2 = 2k\Omega$ results in a gain of 15V/V. While equations 3.3 and 3.4 are not applicable to instrumentation amplifiers due to their 3 op-amp design, the bandwidth can be estimated from the datasheet to be 2.3MHz (as seen in figure 3.3) at the chosen gain. Using equations 3.5 and 3.6, the gain reduction and phase shift at 100kHz can be estimated as -0.004dB and -2.49° respectively. While this still needs to be accounted for during calibration, it represents a very flat and linear response leading to a more accurate system.

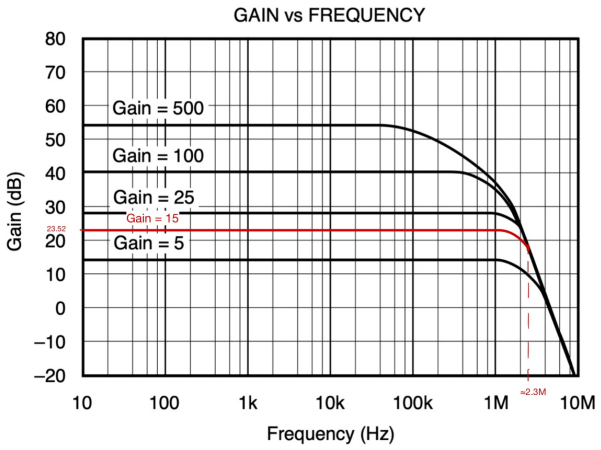

Figure 3.3: INA331 Bandwidth vs Gain adapted from [?]

The second amplification stage uses a TLV9061 op-amp in an inverting gain configuration. With a GBW of 10MHz and gain of $A_v = -20$ ($A_{noise} = 21$) the expected bandwidth is 476.2kHz (equation 3.3). From equations 3.5 and 3.6 an expected -0.094dB gain reduction and -11.86° phase shift is calculated at 100kHz. However, this does not need to be calibrated for as an identical gain stage will be used for the current measurement, ensuring that any gain reductions and phase shifts are cancelled out during impedance calculation.

The final circuit for voltage measurement can be seen in 3.4.

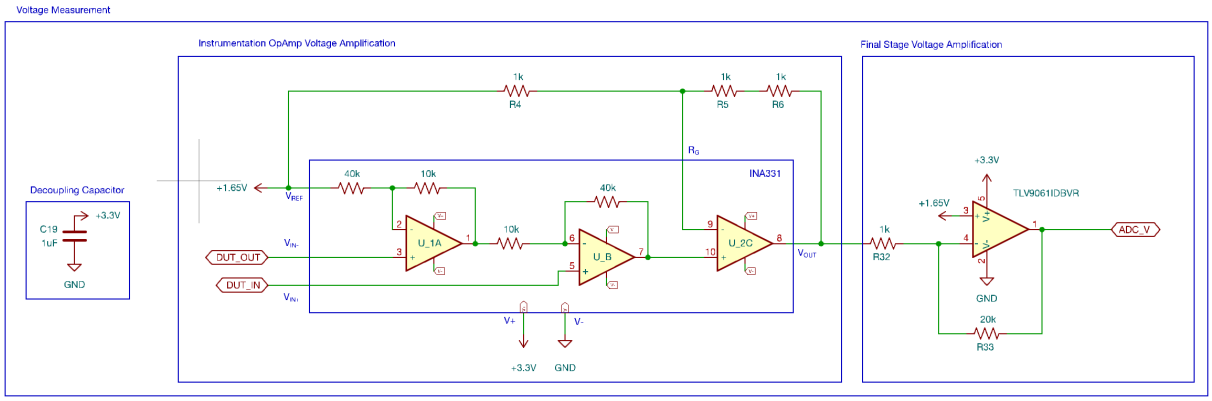

Figure 3.4: Complete Voltage Measurement Stage Circuit

3.3.3. Current Measurement

The most basic method of measuring current is through making use of a precision shunt resistor. This involves placing a small known resistor in series with the current path and measuring the voltage drop across the resistor. Making use of Ohm's Law (equation 3.7), the current can be calculated.

$$V_{drop} = I_{in} \times R_{shunt} \tag{3.7}$$

This approach is cheap and easy to implement, but has severe drawbacks. The voltage drop across the resistor impacts the magnitude of the applied perturbation, thereby impacting the measurements. For biosensing, where signal levels are low, even small drops or error sources can affect sensitivity.

Alternatively a transimpedance amplifier (TIA) can be used. A TIA makes use of the following properties of op-amps:

$$V_n \approx V_p \tag{3.8}$$

$$I_n \approx I_p \approx 0 \tag{3.9}$$

Equation 3.8 shows that the positive input (connected to the DUT) is driven to the same potential as the negative input (the virtual ground reference at 1.65V), thereby ensuring a low-impedance path for the current. Conversely, equation 3.9 ensures that the TIA has a high input-impedance and that the current from the sensor flows entirely through the

feedback resistor. The output voltage is then given by:

$$V_{out} = I_{in} \times R_{feedback} \tag{3.10}$$

The feedback resistor can be large without affecting the applied signal, however it does reduce the bandwidth of the TIA (referring back to equation 3.3). If $R_{feedback}$ is too large, the TIA will experience significant phase shifts and reduced gain at higher frequencies. Similairly to the voltage measurement stage, this can be mitigated by using multiple gain stages.

Additionally, biosensing with a fixed voltage perturbation over a wide impedance range means the current can vary from nanoamps (high impedance, low analyte concentration) to milliamps (low impedance, high analyte concentration). Due to this a fixed gain amplifier is impractical. To achieve accurate measurement across this dynamic range, a programmable gain amplifier (PGA) is used to amplify the TIA output and ensure that the output voltage remains within the optimal range for the ADC. The TIA is also designed with multiple gains by switching the feedback resistor values. This prevents saturation for high currents and maximises resolution for low currents. The result is a three stage current measurement circuit, where the TIA provides the intial current-to-voltage conversion, which is then amplified by a PGA before being amplified by a final inverting gain op-amp. The STM32F303K8 also has an internal PGA with a 8Mhz GBW and binary gains from 2^1 - 2^4. It was unclear wether the added flexibility of a second PGA would outweigh the added noise of an additional gain stage, thus further testing was needed. The PCB was designed with a jumper allowing the internal PGA to be bypassed after testing if needed (see section 3.5).

The OPA3S328 is specifically designed for TIA applications, with a wide GBW of 40MHz, 0.2pA input bias and typical input voltage offset of 10 µV. Importantly it also has integrated switches for switching between feedback resistors. However, the switch on-resistance is non negligable at 90-125Ω and varying with temperature. This will produce gain errors and distortion on the TIA output. This can addressed by using the second switch and op-amp integrated into the OPA3S328 package to build a buffered multiplexer. An example of this circuit is shown in Figure 3.5. The switch is used to sense the TIA output directly at the feedback resistor for each gain, while the second op-amp is used as a buffer. The low input bias current of the op-amp ensures negligable voltage drop (a worst case of 1.25nV), thus providing an accurate Kelvin sense connection. This eliminates the gain error, gain error drift and gain non-linearity due to the switch resistances.

The YBJ variant was chosen due to its 3-way multiplexer (MUX) over the RGR variant with a 2-way MUX, enabling finer gain segmentation and improved measurement precision across the input current range. However, due to the small package size and PCB manufacturing limits (see section 3.5), only two of the three switches were used.

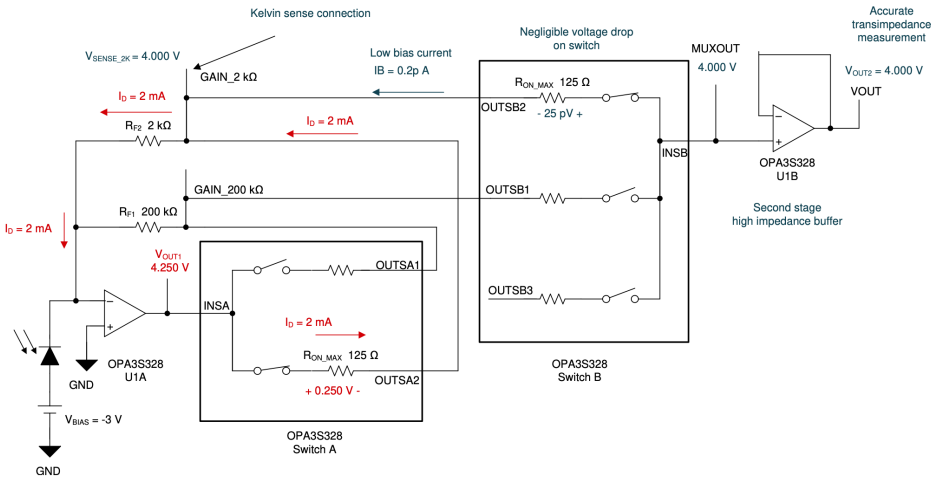

Figure 3.5: Example of Kelvin Sense Switch Connections and High Impedance Buffer [1]

The PGA113 offers gains ranging from 1-200 V/V with a high GBW of 10MHz and is controlled via SPI. It has a low gain error at $\leq 0.3\%$ and extremely low noise at $12\text{nV}/\sqrt{\text{Hz}}$. Combined with a final TLV9061 gain stage (identical to the final voltage measurement stage), this provides variable gain from 20-4000V/V after the TIA. With a further 2-16 V/V provided by the STM's internal PGA if needed, although after testing it was decided that this was not needed. Based on measurements of the biosensor using the PalmSens4, the expected impedance ranges from 100 kΩ at 1Hz to 10 Ω at 100kHz, resulting in a current ranging from 100nA to 1mA. To maximise the ADC's range even at the smallest current, the larger feedback resistor is desgined to deliver 3Vpp at our maximum PGA gain. From equations 3.11 - 3.13, this results in $7.5k\Omega$.

$$V_{TIA} = \frac{3}{4000} = 750\mu V \tag{3.11}$$

$$A_{TIA} = \frac{750\mu V}{100nA} = 7500V/A \tag{3.12}$$

$$\therefore R_{f1} = 7.5k\Omega \tag{3.13}$$

The smaller feedback resistor is then chosen to give the same gain at the maximum PGA gain as the larger resistor gives at the minimum PGA gain, this ensures a smooth transition between feedback resistors with no currents being too large for the larger feedback resistor, but too small for the smaller one. The smaller feedback resistor is then calculated to be 200 times smaller at $R_{f2} = 37.5\Omega$. This ensures that the ranges from 50nA-20μA and 20μA-4mA are covered respectively, while ensuring that the ADC input stays between 1.5-3Vpp.

In traditional TIA designs a capacitor is placed in parallel with the feedback resistor to provide sufficient phase margin and ensure stability [2]. These designs are, however intended for use with a photodiode, rather than EIS. There are few sources available that discuss the design of a TIA for EIS purposes, where capacitance is what is measured rather

than compensated for. These sources do not discuss the necessity of feedback capacitors, thus this has to be derived from theory.

The dominant pole of the open loop response of an op-amp is a function of the GBW and the open loop gain, A_{OL} (equation 3.14). This determines the -3dB frequency of the open loop transfer function and after this point the gain rolls of at a rate of -20dB/decade. Due to the extremely large open loop gains of modern op-amps (130dB or $3.16 \times 10^6 V/V$ for the OPA3S328), negative feedback is required between the output and inverting input. The amount of the output that is fed back to the input is defined as the feedback factor (β) and described by equation 3.15. Where V_{fb} is the voltage present at the inverting input of the op-amp and V_{out} the voltage at the output. This negative feedback results in the closed loop gain (equation 3.16) where the loop-gain refers to $A_{OL} \times \beta$ (equation 3.17).

$$\text{Dominant Pole} = f_{DP} = \frac{\text{GBW}}{A_{OL}} \tag{3.14}$$

$$\text{Feedback Factor} = \beta = \frac{V_{fb}}{V_{out}} \tag{3.15}$$

$$\text{Closed Loop Gain} = A_{CL} = \frac{A_{OL}}{1 + A_{OL}\beta} \tag{3.16}$$

$$\text{Loop Gain} = A_{OL}\beta \tag{3.17}$$

$$\tag{3.18}$$

When the loop-gain is -1, equation 3.16 simplifies to $A_{CL} = \frac{A_{OL}}{0}$ and the system becomes unstable. This happens when V_{fb} leads or lags V_{out} by 180°. The phase margin (PM) is thus defined as in equation 3.19 and describes how close the system is to a 180° phase shift and instability when the loop gain is at 0dB or 1V/V (the critical point or f_c). From equation 3.21 it is shown that this happens when the magnitude plots of A_{OL} and $\frac{1}{\beta}$ intersect. To ensure stability, the PM should be at least 45°, with higher values providing more stability at the cost of transient response [2]. The phase margin can be calculated by subtracting the phase of $\frac{1}{\beta(j\omega)}$ from the phase of $A_{OL}(j\omega)$ to get the phase of $A_{OL}\beta(j\omega)$.

$$\text{PM} = 180° + \varphi_{A_{OL}\beta} \text{ at } |A_{OL}\beta| = 0dB \tag{3.19}$$

$$|A_{OL}\beta| = 0dB = 1V/V \tag{3.20}$$

$$\therefore |A_{OL}| = |\frac{1}{\beta}| \text{ at } f_c \tag{3.21}$$

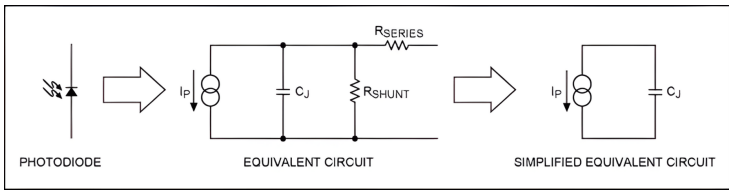

Figure 3.6: Photodiode equivalent circuit [2]

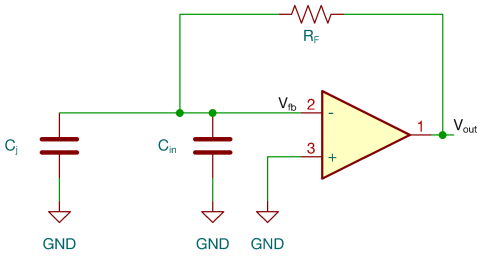

Figure 3.7: Equivalent TIA circuit for photodiodes

$$C_i = C_j + C_{in} \tag{3.22}$$

$$\beta(j\omega) = \frac{X_{c_i}}{R_f + X_{C_i}} = \frac{1}{1 + j\omega R_f C_i} \tag{3.23}$$

$$\therefore \frac{1}{\beta(j\omega)} = 1 + j\omega R_f C_i \tag{3.24}$$

Figure 3.6 shows the simplified equivalent circuit of a photodiode, including the junction capacitance (C_J). With figure 3.7 showing the resulting equivalent circuit model of a TIA for measuring photodiodes, including the input capacitance of the op-amp (C_{in}). From this, the feedback factor can be calculated as seen in equation 3.23. The pole in $\beta(j\omega)$, caused by the combined input capacitance, translates to a zero in $\frac{1}{\beta(j\omega)}$. This zero causes the magnitude of $\frac{1}{\beta(j\omega)}$ to increase at a rate of 20dB/decade after the corner frequency (determined by the value of C_i) and the phase to increase from 0°to 90°. The result is a very small phase margin at the critical frequency and instability (as seen in figure 3.11). The feedback capacitor in parallel with R_f solves this by adding a pole to $\frac{1}{\beta(j\omega)}$, cancelling out the zero and thus adding phase margin.

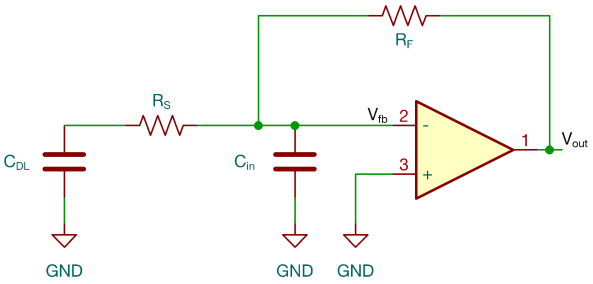

Figure 3.8: Simplified Randles equivalent TIA circuit with ideal capacitance

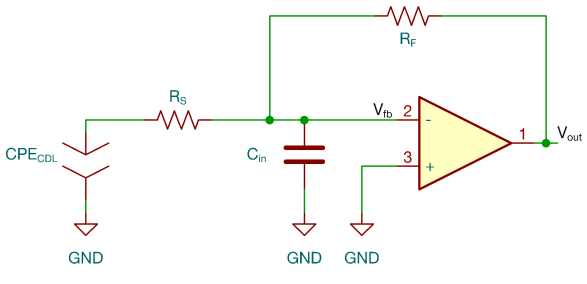

Figure 3.9: Randles equivalent TIA circuit with CPE

Simplified Randles Circuit with Ideal Capacitance:

$$Z_{in} = (R_S + X_{C_{DL}})||X_{C_{in}} \tag{3.25}$$

$$\beta(j\omega) = \frac{Z_{in}}{R_f + Z_{in}} \tag{3.26}$$

$$\therefore \frac{1}{\beta(j\omega)} = 1 + \frac{R_f}{Z_{in}}$$

$$= 1 + \frac{R_f}{(R_S + X_{C_{DL}})||X_{C_{in}}} \tag{3.27}$$

Full Randles Circuit with CPE:

$$Z_{CPE} = \frac{1}{T(j\omega)^{\alpha}} \tag{3.28}$$

$$Z_{in} = (R_S + Z_{CPE})||X_{C_{in}} \tag{3.29}$$

$$\beta(j\omega) = \frac{Z_{in}}{R_f + Z_{in}} \tag{3.30}$$

$$\therefore \frac{1}{\beta(j\omega)} = 1 + \frac{R_f}{Z_{in}}$$

$$= 1 + \frac{R_f}{(R_S + Z_{CPE})||X_{C_{in}}} \tag{3.31}$$

However, the equivalent Randles circuit model of a biosensor differs fundamentally from the model of a photodiode due to the series resistance R_s. Figures 3.9 and 3.8 show the equivalent TIA circuits for a non-faradaic Randles circuit and a simplified model using an ideal capacitance (C_{dl}) instead of the CPE by approximating $T = C_{dl}$ and $\alpha = 1$. For the simplified model, the input impedance and feedback factor can be calculated as seen in equations 3.25 - 3.26. The full Randles non faradaic equivalent circuit results in 3.30. The series resistance and double layer capacitance of the biosensor was estimated using PS Trace and values for input capacitance, open loop gain and gain bandwidth were read from the OPA3S328 datsheet. A MatLab script was then used to calculate the $\frac{1}{\beta(j\omega)}$ transfer function and loop gain of the system. Similairly the series resistance, T and α values were estimated for the Randles circuit using circuit fitting in PS Trace and plotted in MatLab. The response of the equivalent photodiode model was also plotted using the constant C_{DL} as the parasitic junction capacitance. Table 3.1 shows the estimated circuit paramaters and figures 3.11 and 3.10 shows the resulting responses. Table 3.2 lists the calculated critical frequencies and phase margins.

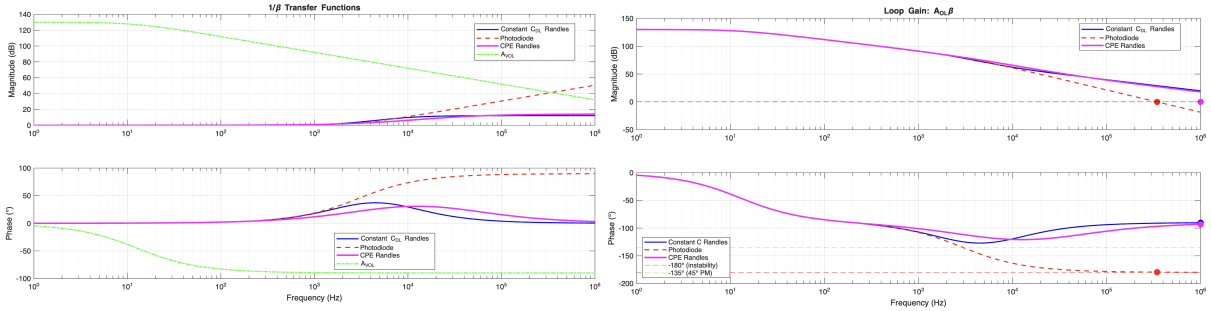

(a) $\frac{1}{\beta(j\omega)}$ frequency response **(b)** Loop Gain frequency response

Figure 3.10: Calculated frequency responses for $R_F = 37.5\Omega$

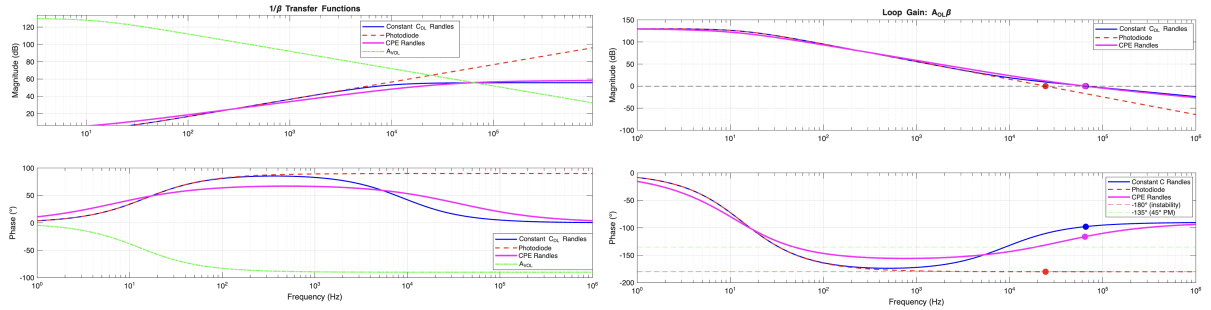

(a) $\frac{1}{\beta(j\omega)}$ frequency response **(b)** Loop Gain frequency response

Figure 3.11: Calculated frequency responses for $R_F = 7.5k\Omega$

From these plots, the difference between the photodiode and biosensor circuits become clear. At low frequencies the simplified biosensor circuit closely follows the response of the photodiode. This is due to the zero caused by the capacitance dominating the response ($X_{C_{DL}} >> R_S$) and thus the equivalent circuits of the photodiode and Randles circuit are near identical. However, at higher frequencies R_S becomes much larger than $X_{C_{DL}}$ and the responses start to diverge. The dominance of R_S at higher frequencies ensure that ample phase margin is achieved by the critical frequency. The full Randles non-faradaic circuit model provides a more accurate representation of the biosensor TIA circuit and diverges earlier than the simplified circuit due to the CPE. This confirms that ample phase margin is available at both $R_f = 37.5\Omega$ and $R_f = 7.5k\Omega$, meaning that no feedback capacitors are needed. At extremely large values of R_F the phase margin reduces, and the system can become unstable ($R_f > 40k\Omega$ for this circuit). Since adding compensation capacitors reduces the bandwidth of the TIA [2], it is not recommended for biosensing TIA circuits, except in cases of extremely high feedback resistor values.

Table 3.1: Circuit Parameters

Parameter	Value
CPE Randles Circuit	
R_S	8.975 Ω
T	6.993×10^{-6}
α	0.785
C_{in}	4.0 pF
Constant C Randles Circuit	
R_S	12.3 Ω
C_{DL}	1436.0 nF
C_{in}	4.0 pF
Photodiode Equivalent	
C_i	1436.0 nF

Table 3.2: Stability Analysis Results

Configuration	f_c (kHz)	PM (°)	Status
$R_f = 7.5\,\text{k}\Omega$			
Constant C Randles	65.83	82.2	Stable
Photodiode	24.22	0.1	Unstable
CPE Randles	64.22	63.8	Stable
$R_f = 37.5\,\Omega$			
Constant C Randles	9840.03	89.8	Stable
Photodiode	343.77	0.5	Unstable
CPE Randles	7725.81	86.3	Stable

The final current measurement circuit is shown in Figure 3.12.

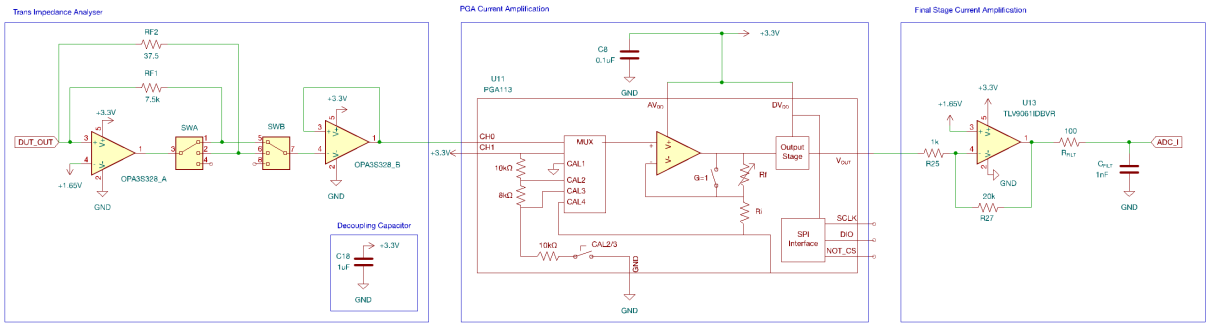

Figure 3.12: Complete Current Measurement Stage Circuit

3.3.4. DUT

The design and manufacture of biosensors are outside the scope of this project. The biosensors described in [23] were used for this project, however the system could easily be adapted to work with other capacitive biosensors. To ensure ease-of-use, a method of interfacing with the biosensors that is simple and reliable needed to be developed. Spring-loaded battery connectors were used as they allow the DUT to be easily slid in and out of the device when combined with a 3d printed enclosure.

Insert 3d model of connectors, dut and 3d print.

3.3.5. Multiplexer

Two approaches towards multiplexing were considered. One approach is to have multiple excitation sources and measurement stages, allowing for simultaneous measurements of all

DUTs. This approach has the advantage of speeding up the measurement process, while allowing each DUT to have electronics dedicated to its measurement range. The major disadvantages to this approach is complexity and cost.

Another approach is re-using the same excitation and measurement circuitry, by switching the input and outputs between the DUTs. This reduces the cost and complexity, but is reliant on having a reliable switching mechanism that does not impact the measurements.

Ultimately the best approach was using a single set of excitation and measurement circuitry, multiplexed in order to measure DUTs sequentially. The cost reductions of this approach outweighs the increased measurement time as no user input is required between DUT measurements.

Various options for multiplexers were considered including dedicated analogue multiplexers (MUX ICs), op-amp based multiplexers and relays. Dedicated analogue multiplexers consist of a collection of analogue switches. They typically use CMOS technology, resulting in compact integration and fast switching speeds. Modern analogue switches are available with very low on-resistance ($< 1\Omega$) and a high degree of flatness [31]. However, leakage currents are inherent to these solid-state devices and can corrupt low-current signals, especially in the nanoampere range [31].

Op-amp-based multiplexers such as seen in Figure 3.13 provide buffering and impedance matching, which make them ideal for multiplexing voltage signals, but the buffering also make them unsuitable for use with current signals.

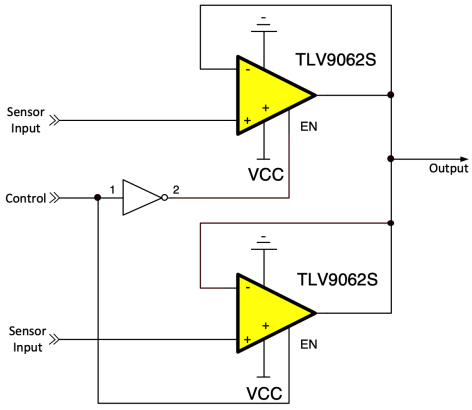

Figure 3.13: Op-amp based multiplexer circuit [3]

Signal relays, in contrast, use electromechanical contacts to physically open or close signal paths, offering near-zero leakage current and extremely low, stable contact resistance that is independent of signal voltage and temperature. This physical isolation and connection ensures that the measured current accurately reflects the biosensor response. While relays are slower to switch and larger than solid-state alternatives, their switching speed is more than sufficient for switching between sensors.

The TXS2-L2-3V DPDT latching signal relay was chosen due to its small size, low

operating current (23.3 mA) and high mechanical lifetime (Minimum 200 000 operations). The major concern of a mechanical relay is the mechanical wear, however at an assumed 2 actuations per measurement and 50 measurements a day, the relays are expected to last more than 5 years. Utilising the DPDT topology of the relay, they can be configured in a tree pattern, allowing for 4 DUT's to be switched using 3 relays as seen in figure 3.14.

Despite the low operating current, a driver circuit is still needed to power the relay from a microcontroller GPIO. This consists of a lowside NPN transistor and a flyback diode to protect against voltage spikes when the coil is switched off. The final circuit can be seen in figure 3.15

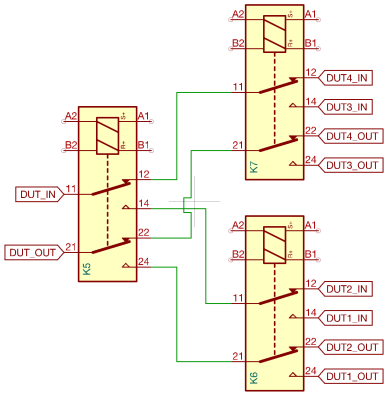

Figure 3.14: Relay Multiplexer Topology for 4 DUT's

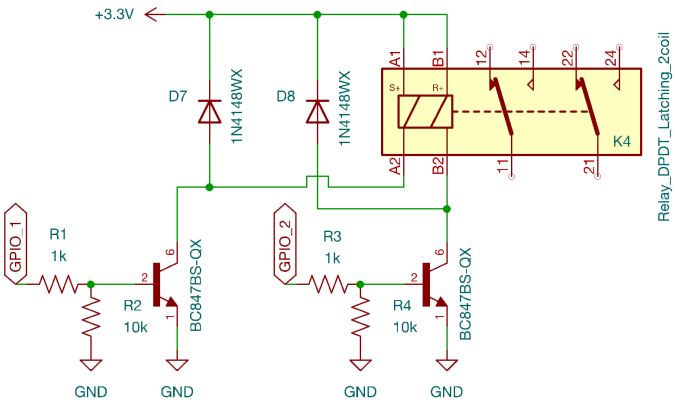

Figure 3.15: Relay Driver Circuit for one relay

3.3.6. Power Circuitry

With portability in mind, a battery is a requirement for the system. It was decided that the most cost-effective approach would be to utilise a microcontroller with built-in LiPo charging circuitry instead of a dedicated charging circuit as this is commonly available in many ESP32 boards. The 3.3V rail from the ESP will then be used to power the rest of the system.

As mentioned in Section 3.3.1, a 1.65V reference is needed for the analogue circuitry. Due to the small amplitude of the excitation signal, it needs to be highly accurate and stable. This was done through the use of a matched resistor array and a op-amp buffer. Using a resistor array ensures that our reference is the exact midpoint of the supply voltage despite any tolerances in the precise resistor value, while the op-amp buffers this output to avoid loading the resistor array and causing a voltage drop. Choosing a too large resistor value risks a slightly uneven voltage drop due to the input bias current of the op-amp buffer, on the other hand, a lower value increases the static current draw and power consumption. $1k\Omega$ was chosen as a balance between these tradeoffs.

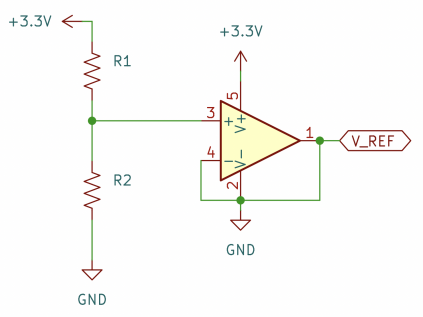

Figure 3.16: Virtual ground reference circuit

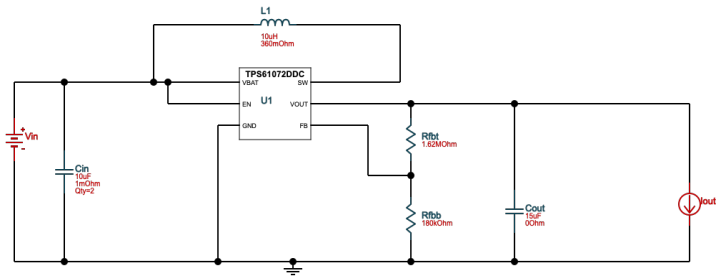

Figure 3.17: 5V boost converter circuit

The LTC1069 AA-Filter requires a 5V supply voltage. A 3.3V to 5V boost circuit was designed around the TPS61072 boost regulator using the TI WeBench power supply design tool [32], ensuring a stable and efficient circuit as seen in figure 3.17.

3.3.7. Signal Processing

3.3.8. User Interface

Fill in once GUI is actually done Talk about flexibility of having both physical buttons and display aswell as web ui, allowing both standalone use and use with either computer, tablet or cell phone, ensuring versatility across environments

3.4. Circuit Simulation

3.4.1. Biosensor

Despite the widespread use of CPEs in electrical simulations, the SPICE family of simulators lack a native CPE element. There are a variety of approaches to modelling CPEs such as Laplace transform, Fourier theory or using a network of resistors and capacitors. [33] builds on existing approaches to modelling a CPE using a combination of resistors and capacitors (such as Add references from wilson), by using an array of parallel RC elements as seen in Fig **??**. The branches form a theoretically infinite geometric progression of characteristic frequencies [33], however characteristic frequencies above and below the frequency range of interest are approximated using a single capacitor and resistor respectively. [33] provides MatLab code that calculates the R and C values of all the branches and this was used to model a CPE element matching the biosensor in LTSpice. Figure **??** shows that the CPE model does indeed exhibit a constant phase across the measurement range of interest (1Hz-100kHz) and figure **??** shows the simulated response of the biosensor including R_S.

Comparing this to the PalmSens measurements (figure **??**) shows that this model serves as a fairly accurate representation of the DUT for simulation purposes.

3.4.2. Excitation stage

For the simulation of the excitation stage, a sample-and-hold block was used to mimic the DAC at varying sample rates. LTSpice has no included components to simulate a raised cosine filter, thus a FIR filter block from [34] with a raised cosine response and $\beta = 1$ was used. Comparing the simulated frequency response with the LTC1069-7 datasheet (Figures 3.18 and 3.19) for cutoff frequencies of 10kHz and 100kHz, the overall magnitude response is a good approximation, despite some differences at high levels of attenuation ($< -50dB$). The simulated phase response, however is non-linear which does not match the LTC1069-7, but this will not impact the overall system simulation as the DUT is being excited at a single frequency. The TLV9061, INA331 and OPA3s328 PSpice models were obtained from TI and adapted to work in LT Spice. The TLV9061 was used for the attenuation stage.

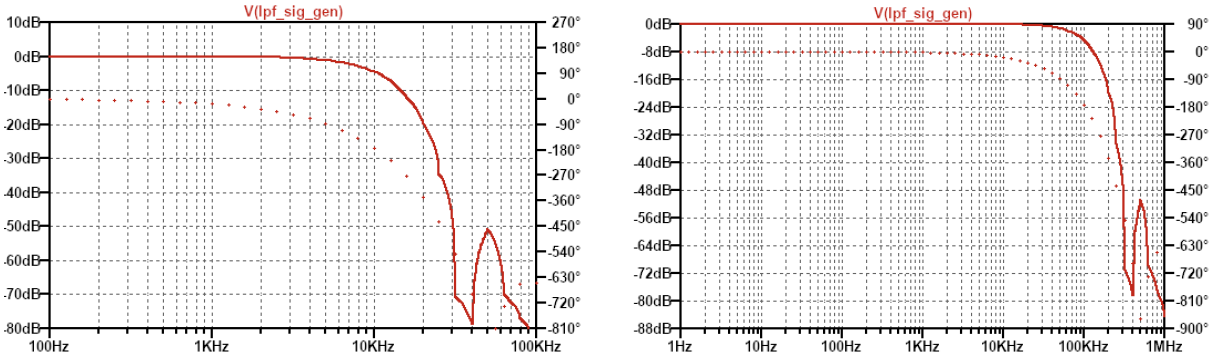

(a) 10kHz cutoff frequency **(b)** 100kHz cutoff frequency

Figure 3.18: Simulated FIR filter frequency responses

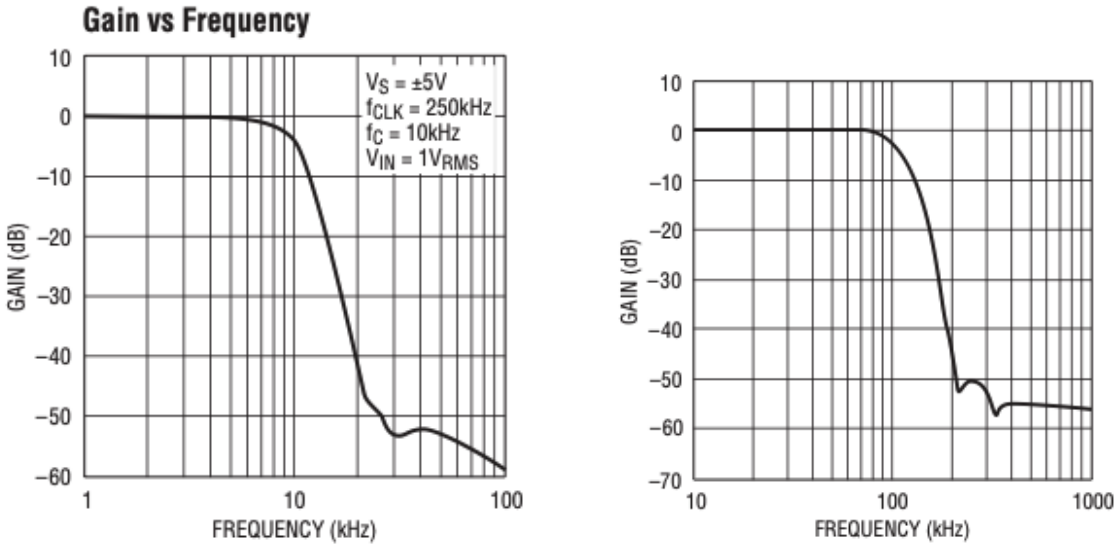

(a) 10kHz cutoff frequency **(b)** 100kHz cutoff frequency

Figure 3.19: LTC1069-7 datasheet frequency responses

Figure 3.20a shows a 10kHz signal with 32x oversampling generated by the DAC before and after passing through the AA-filter and after being attenuated. Figure **??** shows current through the simulated DUT resulting from this signal.

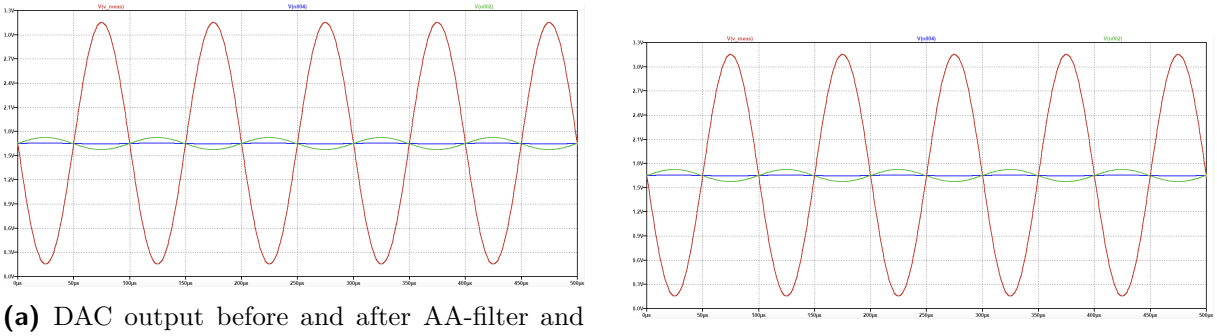

(a) DAC output before and after AA-filter and attenuation **(b)** Current through simulated DUT

Figure 3.20: Simulated excitation stage output and DUT response

3.4.3. Voltage measurement

The voltage measurement stage was simulated with the INA331 and TLV9061 models to confirm the frequency response of the system. Figure 3.21 shows only a slight gain reduction of -0.02dB gain reduction at 100kHz and a -4.6°phase shift. Fig 3.22 shows the overall frequency response of the voltage measurement stage with the TLV9061 amplification stage contributing an additional -0.2dB gain reduction and -3.4°phase shift. This confirms that sufficient bandwidth is available for measurements up to 100kHz.

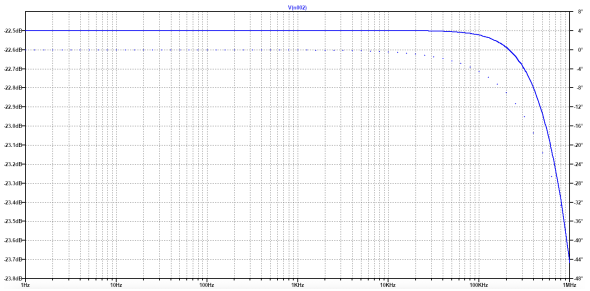

Figure 3.21: INA331 frequency response

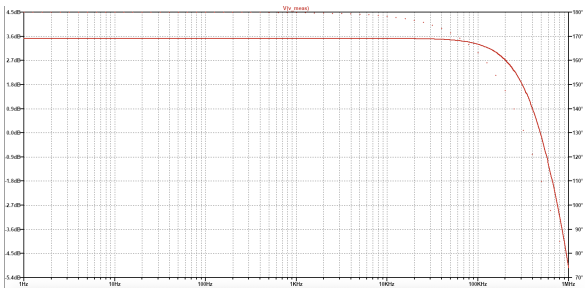

Figure 3.22: Complete voltage measurement stage frequency response

3.4.4. Current measurement

Due to problems porting the OPA3s328 PSpice model to LT Spice, the internal mux was not simulated. The PGA113 has no available PSpice model [35], thus a standard inverting amplifier configuration using the TLV9061 was used to simulate the PGA stage. Figure **??** shows the frequency response of the TIA stage alone, with a -0.15dB gain reduction and -7.2°phase shift at 100kHz. Figure **??** shows the overall frequency response of the current measurement stage with the PGA and final amplification stages contributing an additional -0.25dB gain reduction and -4.8°phase shift. This confirms that sufficient bandwidth is available for measurements up to 100kHz.

To confirm the stability of the TIA circuit, Tian's method was used to plot the loop gain and phase margin for both the Radnles circuit using the CPE and the simplified circuit using a constant capacitance as seen in figure **??** and Table **??**. These results closely match the MatLab results in section 3.3.3, confirming that the TIA design is stable without the need for feedback compensation.

3.4.5. Complete System

The individual subsystems were combined into a complete model including DAC and ADCs using sample-and-hold blocks. Transient analysis was done at a range of excitation frequencies. For frequency analysis the DAC and ADCs were excluded.

3.5. PCB Design

Beskryf filosofie en idees wat mee ingegaa het. Briefly discuss general PCB design principles wat design geguide het (Analogue ground plane etc). Beskryf beperkings van PCB manufactures wat inag geneem moes word (PCB size, layers, trace width via diamtre etc.). Noem briefly hoekom PCB in China eerder as Uni laat maak. Gaan deur design logic en discuss probleem met TIA. Include maybe final PCB diagram en langs dit foto van manufactured PCB.

All PCB design was done using KiCad due to its open-source nature and wide usage in industry. Due to the complexity of the circuit, JLC PCB was used for manufacturing rather than Stellenbosch University's in-house PCB manufacturing. There are substantial price differences between JLC's standard process and their more advanced processes ($4 vs $68). Table 3.3 lists the key limits of JLC's standard PCB process that had to be taken into account.

Another key consideration when designing the PCB was minimising noise and interference in the analogue circuitry. Given the limitations of a two-layer PCB, maintaining a continuous and low-impedance ground reference was a key priority, as a fully dedicated ground plane was not practical. To achieve this, both layers incorporated extensive ground copper pours connected through frequent stitching vias to minimise loop inductance and reduce electromagnetic interference (EMI) coupling between layers. A single unified ground network was chosen over separate analogue and digital grounds, as is modern best practice for low-current mixed-signal systems [36]. Instead, the analogue and digital sections were physically partitioned, with sensitive analogue components and signal routed away from high-speed digital traces. Fencing vias were deployed along region boundaries to confine high-frequency digital currents and provide additional shielding for low-level analogue signals (Figure **??**).

Subsystems we're grouped together with jumpers connecting subsystems, allowing for easier debugging and testing. Care had to be taken in selecting the pin usage for both the STM32 and ESP32 as nearly all pins on both devices were used. The small package size of the OPA3S328 (24-pin DSBGA with 0.4 mm pitch) also posed challenges for routing. With a minimum pad diameter of 0.25 mm and 0.4 mm pitch, the clearance between pads is only 0.15 mm, meaning that traces could not be routed between pads. Usually this would be solved using via-in-pads, however, the minimum via hole diameter of 0.3 mm meant that this was not possible with JLC's low cost PCB manufacturing process. By only using 2 of the 3 internal switches, OUTSB3 could be used to route the common node of switch B to the non inverting input of the buffer op-amp (Figure 3.25). This reduced the number of gain settings to 2 as mentioned in section 3.3.3.

The complete PCB schematic is shown in Appendix **??** and the final PCB layout in Figure 3.24.

Table 3.3: JLC PCB Standard Manufacturing Process Limits

Parameter	Limit
Minimum Trace Width	0.1 mm (4 mil)
Minimum Trace Spacing	0.1 mm (4 mil)
Minimum Via Diameter	0.45 mm
Minimum Via Hole Diameter	0.3 mm
Minimum BGA Pad Diameter	0.25 mm
Maximum Board Size	100 mm × 1100 mm
Number of Layers	2, 4, or 6 layers

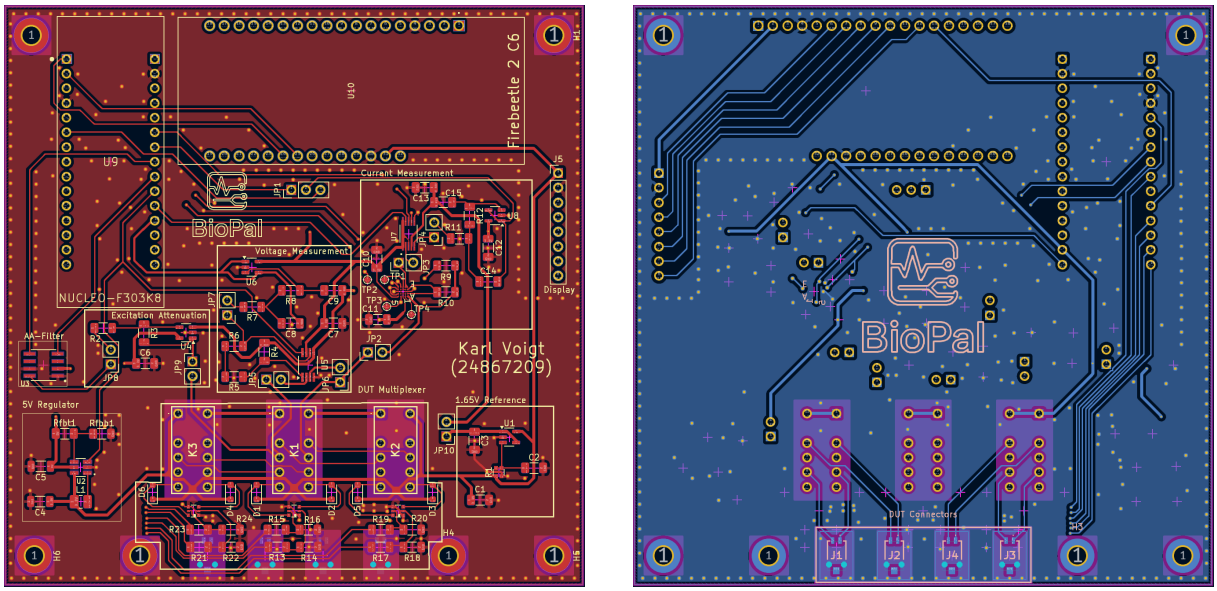

(a) PCB front layout

(b) PCB back layout

Figure 3.23: Final PCB layout

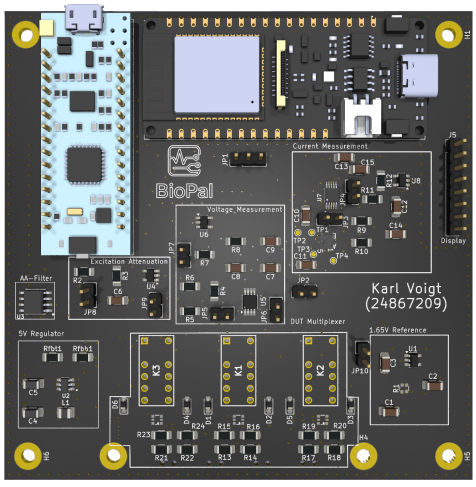

Figure 3.24: Final PCB render

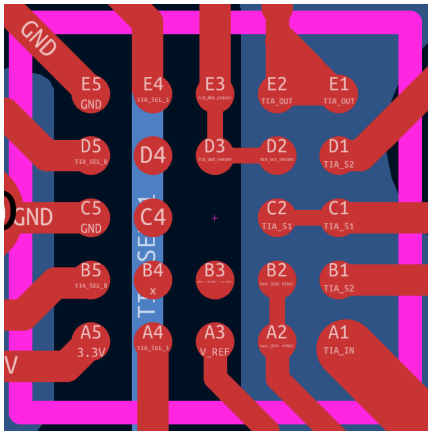

Figure 3.25: OPA3S328 BGA routing solution

3.6. Firmware Design

Inculde flow diagram.

3.6.1. ESP

Vertel van wat ons wil bereik en hoekom. Discuss libraries used. Discuss maybe issues rondom C6 en hoe dit gesolve is en hoekom die C6 steeds die rgete keuse was.

3.6.2. STM

Probleme met arm library te groot. Discuss met flow chart hoe DMA en als met DAC en ADC interact en dan UART en badies program flow. Delve into limits van STM en maybe briefly setup van DAC en ADC.

Chapter 4

Testing & Validation

4.1. PCB Testing

4.1.1. Voltage Reference Load Testing

4.1.2. Excitation Stage Testing

4.1.3. Voltage Measurement Testing

4.1.4. Current Measurement Testing

4.1.5. Multiplexing Testing

4.1.6. Complete System Test Without & With MCU

4.2. Validation

4.2.1. Test on Calibration Cell

4.2.2. Test on Saline Solution

4.2.3. Discussion of Results

Chapter 5

Summary and Conclusion

Bibliography

[1] L. Chioye, "Build a Programmable Gain Transimpedance Amplifier Using the OPA3S328," 2021.

[2] "Stabilize Your Transimpedance Amplifier | Analog Devices," https://www.analog.com/en/resources/technical-articles/stabilize-transimpedance-amplifier-circuit-design.html.

[3] "Sboa311a."

[4] N. Bhalla, P. Jolly, N. Formisano, and P. Estrela, "Introduction to biosensors," *Essays in Biochemistry*, vol. 60, no. 1, pp. 1–1, Jun. 2016.

[5] "Biomarkers | National Institute of Environmental Health Sciences."

[6] A. Rosenzweig, "What Are Pancreatic Cancer Biomarkers? - Pancreatic Cancer Action Network," 2018.

[7] J. A. Ribeiro and P. A. Jorge, "Applications of electrochemical impedance spectroscopy in disease diagnosis—A review," *Sensors and Actuators Reports*, vol. 8, pp. 100 205–100 205, Dec. 2024.

[8] X. Zeng, Z. Shen, and R. Mernaugh, "Recombinant antibodies and their use in biosensors," *Analytical and bioanalytical chemistry*, vol. 402, no. 10, pp. 3027–3038, Apr. 2012.

[9] S. Sueda, "Antibody immobilization for immunosensing," *Analytical Sciences*, vol. 38, no. 1, pp. 1–2, Jan. 2022.

[10] "Using Antibodies as vaccine delivery vehicles," https://downhousesoftware.wordpress.com/2013/12/.

[11] J. S. Daniels and N. Pourmand, "Label-Free Impedance Biosensors: Opportunities and Challenges," *Electroanalysis*, vol. 19, no. 12, pp. 1239–1257, 2007.

[12] H. S. Magar, R. Y. A. Hassan, and A. Mulchandani, "Electrochemical Impedance Spectroscopy (EIS): Principles, Construction, and Biosensing Applications," *Sensors*, vol. 21, no. 19, p. 6578, Jan. 2021.

[13] A. C. Lazanas and M. I. Prodromidis, "Erratum: Electrochemical Impedance Spectroscopy-A Tutorial (ACS Measurement Science Au (2023) 3:3 (162-193) DOI: 10.1021/acsmeasuresciau.2c00070)," *ACS Measurement Science Au*, vol. 2023, no. 3, pp. 14–14, 2025.

[14] "EIS Quality Indicators and Linearity Correction."

[15] Q.-Z. Xie, M.-W. Lin, E.-W. Hsu, and C.-T. Lin, "Review—Advancements of Nanoscale Structures and Materials in Impedimetric Biosensing Technologies," *ECS Journal of Solid State Science and Technology*, vol. 9, p. 115027, Oct. 2020.

[16] "Bode and Nyquist Plot."

[17] L. A. Buscaglia, J. P. Carmo, and O. N. Oliveira, "Simple-Z: A Low-Cost Portable Impedance Analyzer," *IEEE Sensors Journal*, vol. 23, no. 21, pp. 26 067–26 074, Nov. 2023.

[18] A. Al-Ali, A. Elwakil, A. Ahmad, and B. Maundy, "Design of a Portable Low-Cost Impedance Analyzer," *BIODEVICES 2017 - 10th International Conference on Biomedical Electronics and Devices, Proceedings; Part of 10th International Joint Conference on Biomedical Engineering Systems and Technologies, BIOSTEC 2017*, vol. 2, pp. 104–109, Feb. 2017.

[19] M. Ibrahim, "CMOS Transimpedance Amplifier for Biosensor Signal Acquisition."

[20] ""Improved" Howland current pump circuit," 2020.

[21] T. Brown, "Design Thinking," *Harvard Business Review*, Jul. 2008.

[22] "PalmSens4," https://www.palmsens.com/product/palmsens4/.

[23] T. Ebrahim, "The development of a biosensor for the early detection of pancreatic cancer," 2023.

[24] C. Dincer, R. Bruch, A. Kling, P. S. Dittrich, and G. A. Urban, "Multiplexed Point-of-Care Testing – xPOCT," *Trends in Biotechnology*, vol. 35, no. 8, pp. 728–742, Aug. 2017.

[25] L. Gaddy and H. Kawai, "DYNAMIC PERFORMANCE TESTING OF DIGITAL AUDIO D/A CONVERTERS."

[26] "LTC1069-7CS8#PBF," https://www.digikey.co.za/en/products/detail/analog-devices-inc/LTC1069-7CS8-PBF/889060.

[27] e. technology, "What are the Drawbacks of Differential Amplifier Circuits?" https://www.eimtechnology.com/blogs/articles/what-are-the-drawbacks-of-differential-amplifier-circuits, Apr. 2024.

[28] "The Instrumentation Amplifier | Operational Amplifiers | Electronics Textbook," https://www.allaboutcircuits.com/textbook/semiconductors/chpt-8/the-instrumentation-amplifier/.

[29] J. M. Fiore, "5.3: Gain-Bandwidth Product," in *Operational Amplifiers and Linear Integrated Circuits - Theory and Application (Fiore)*, May 2018.

[30] M. Oljaca and H. Surtihadi, "Operational amplifier gain stability, Part 1: General system analysis," 2010.

[31] "Selecting the Right CMOS Analog Switch | Analog Devices," https://www.analog.com/en/resources/design-notes/selecting-the-right-cmos-analog-switch.html.

[32] "WEBENCH-CIRCUIT-DESIGNER Design tool | TI.com," https://www.ti.com/tool/WEBENCH-CIRCUIT-DESIGNER.

[33] M. Wilson, L. Cowie, V. Farrow, M. Cree, and J. Scott, *Simulating Fractional Capacitors with the SPICE Circuit Simulator*, Sep. 2023.

[34] "Filter manual," http://ltspicegoodies.ltwiki.org/FilterManual.php#FIR_examples.

[35] "PGA113 Pspice model - Logic forum - Logic - TI E2E support forums," https://e2e.ti.com/support/logic-group/logic/f/logic-forum/1178762/pga113-pspice-model, Dec. 2022.

[36] "What Are the Basic Guidelines for Layout Design of Mixed-Signal PCBs? | Analog Devices," https://www.analog.com/en/resources/analog-dialogue/articles/what-are-the-basic-guidelines-for-layout-design-of-mixed-signal-pcbs.html.

Appendix A

Project Planning Schedule

This is an appendix.

Appendix B

Outcomes Compliance

This is another appendix.